RSC Advances

PAPER

View Article Online
View Journal | View Issue



Cite this: *RSC Adv.*, 2020, **10**, 34187

# An amine-bifunctionalization strategy with Beta/KIT-6 composite as a support for $CO_2$ adsorbent preparation

Yuan Yuan, Jianwen Wei,* Linlin Geng, Dejun Mei and Lei Liao*

An amine-bifunctionalized composite strategy was used to fabricate grafted-impregnated micro-/mesoporous composites for carbon dioxide capture. The micro-/mesoporous Beta/KIT-6 (BK) composite containing a high-silica zeolite with a three-dimensional twelve-membered ring crossing channel system and cubic structural silica was used as a support, and 3-aminopropyltrimethoxysilane (APTS) and tetraethylenepentamine (TEPA) were used as the grafted and impregnated components, respectively. The amine efficiency, adsorption kinetics, thermal stability, regeneration performance, and the effects of impregnated amine loadings (30–60%) and temperatures (40–90 °C) on the $CO_2$ adsorption performance were investigated using a thermal gravimetric analyzer (TGA) in the mixed gases (15 vol% $CO_2$ and 85 vol% $N_2$). At 60 °C, the bifunctionalized Beta/KIT-6 (1 mL APTS $g^{-1}$ BK) displayed the highest $CO_2$ adsorption capacity of 5.12 mmol $g^{-1}$ at a TEPA loading of 50%. The kinetic model fitting results showed that the $CO_2$ adsorption process was a combination of physical and chemical adsorption, wherein the chemical adsorption is dominant. After five adsorption/desorption cycle regenerations, the saturated adsorption capacity of the composite material was 4.86 mmol $g^{-1}$, which was only 5.1% lower than the original adsorption capacity. The composites demonstrated excellent $CO_2$ adsorption performance, indicating the promising future of these adsorbents for $CO_2$ capture from actual flue gas after desulfurization.

Received 8th June 2020
Accepted 10th September 2020

DOI: 10.1039/d0ra05044j

rsc.li/rsc-advances



## Introduction

Global warming and extreme weather occurrences are caused by the rapid increase of greenhouse gases (GHGs) in the atmosphere.[1] Among them, the main reason for the large amount of $CO_2$ emitted into the atmosphere is the high demand for fossil fuels (coal, oil, natural gas).[2] Carbon dioxide capture and storage (CCS) technology is an effective way for $CO_2$ emission reduction.[3] Absorption of aqueous solutions of amines,[4] porous material adsorption,[5] cryogenic distillation,[6] and membrane separation[7] are the main methods of $CO_2$ recovery. Solid adsorption has been regarded as one of the most promising $CO_2$ capture methods due to the advantages of high $CO_2$ selectivity, renewable cycle performance, rapid rate of adsorption/desorption, low price and little corrosion.[8] The solid adsorbents commonly used in $CO_2$ capture include carbon-based materials,[9] zeolite molecular sieves,[10] metal–organic frameworks (MOFs)[11] and hydrotalcites.[12] According to the study of Abanades *et al.*, it can be calculated that the cost of removing $CO_2$ from zeolites is the lowest, compared with monoethanolamine and active carbons.[13] As $CO_2$ adsorbents, the microporous zeolite molecular sieves mainly consist of 13X,[14] Beta,[15] ZSM-5,[16] Y-type[17] and MER-type,[18] while the mesoporous molecular sieves include MCM series,[19] SBA series,[20] and KIT series.[21] Microporous zeolite has excellent stability but small pore size, which leads to slow molecular escape rate;[22] the pore wall of mesoporous molecular sieves with large pore size is thin and non-crystalline, and may collapse at high temperature.[23] Therefore, the preparation of dual structural micro-/mesoporous composite molecular sieves has attracted the attention of researchers. Guo *et al.* synthesized the Beta/MCM-41 composite through a "two-step method" crystallization process combining a low crystalline Beta zeolite synthetic gel with CTAB, and the result showed that the composite possessed a well-ordered mesoporous MCM-41 phase and a Beta zeolite phase.[24] Using hydrothermal crystallization, Zhang *et al.* fabricated the composite material Y/MCM-48 with significantly improved thermal stability and acidity.[25] At the same time, in order to further improve the adsorption performance of $CO_2$, amino-modified zeolite materials have attracted more and more scholars' attention, and the common modification methods of amino-group are divided into impregnation[26] and grafting.[27] Grafting modified molecular sieves can avoid the high reaction temperature required for the water removal and improve the selectivity and thermal stability of $CO_2$, however, the number of amino groups introduced is less than that of the impregnation

*Guangxi Scientific Experiment Center of Mining, Metallurgy and Environment, Guilin University of Technology, Guilin 541004, PR China. E-mail: jianwen988@126.com; 976285986@qq.com*

method. Therefore, researchers have combined the two methods in recent years. Wang *et al.* impregnated various amounts of TEPA onto the MCM-41 grafted by APTS and found that the new adsorbent could promote $CO_2$ adsorption, with the maximum adsorption capacity of 3.5 mmol $g^{-1}$.[28] Sanz-Pérez *et al.* impregnated TEPA, polyethyleneimine (PEI) and piperazine (PZ) on the SBA-15 modified by APTS grafting, respectively.[29] The results showed that the $CO_2$ adsorption capacity of TEPA impregnated carrier was higher than that of carrier with better cycling stability. At 45 °C and 1 atm, the corresponding adsorption capacity was 2.4 mmol $g^{-1}$ and the amine efficiency was 0.32 mol $CO_2$ $mol^{-1}$ N. At present, the $CO_2$ adsorption by amine-bifunctionalized micro-/mesoporous composite molecular sieves is still at the exploratory stage, and the combination of molecular sieves with different pore sizes, organic amine's types, amine efficiency and cyclic stability of the materials are all research hotspots. Beta is a kind of high-silicon zeolite with three-dimensional twelve-membered ring crossing channel system. Compared with 1D arranged MCM-41 and 2D arranged SBA-15, KIT-6 with 3D pore arrangement exhibits the distinct mass transfer performance because of its large pore diameter as well as pore volume.[30] In this work, Beta/KIT-6 composite was prepared by post synthesis, while APTS and TEPA were grafted and impregnated on Beta/KIT-6, respectively, using the "two-step method", which has not been reported for $CO_2$ adsorption. Characteristics of composite Beta/KIT-6, APTS-Beta/KIT-6 and APTS-Beta/KIT-6-TEPA, and the adsorption mechanism of $CO_2$ were investigated. The adsorption performance test of $CO_2$ was carried out in the simulated flue gas conditions of 60 °C and 15 vol% $CO_2$.

# Experimental

### Preparation of support

For the Beta microporous molecular sieve, 29.45 g tetraethyl ammonium hydroxide (TEAOH, 25 wt%, Aladdin Industrial Co., Shanghai, China) and 21.43 g tetraethyl orthosilicate (TEOS, Aladdin Industrial Co., Shanghai, China) were stirred well at room temperature (350 rpm). The mixed solution was designated as S1. 0.19 g sodium hydroxide (NaOH, Aladdin Industrial Co., Shanghai, China), 0.76 g sodium metaaluminate ($NaAlO_2$, Aladdin Industrial Co., Shanghai, China), 3.5 g TEAOH, and 2 g deionized water ($H_2O$) were mixed and stirred in a beaker until dissolved, and the mixed solution was designated as S2. Then, S2 was added dropwise to S1 and stirred for 4 h until the sol formed was no longer delaminated. The Beta molecular sieve was obtained by high-pressure reaction (140 °C, 24 h), centrifugal separation, drying (80 °C, 10 h) and calcination (550 °C, 6 h). Under atmospheric pressure, the typical post synthesis method was used to synthesize the Beta/KIT-6 composite molecular sieve.[31] First, for the KIT-6, 4 g P123 (Aladdin Industrial Co., Shanghai, China) and 6.7 mL HCl (AR, Sinopharm Chemical Reagent Co., Ltd, Shanghai, China) were dissolved in 144 mL $H_2O$ and stirred at 35 °C for 2 h until P123 dissolves completely. Next, 4.94 mL BuOH (Xilong Chem. Reagent Co., Shantou, China) were added in a slow drip and then stirred for 1 h; 9.24 mL TEOS were added to the solution, and stirred at a 40 °C for 24 h. Then, the pure KIT-6, was obtained by hydrothermal reaction (100 °C, 24 h), vacuum suction filtration, drying (100 °C, 24 h) and calcination (550 °C, 6 h).[32] Second, for the Beta/KIT-6 composite molecular sieve, which was recorded as BK, according to the above production steps of KIT-6, after P123 was completely dissolved, 1.5 g Beta molecular sieve prepared in advance were added and stirred for 1 h, and the rest of the steps were the same.

### Preparation of amine bifunctionalized samples

APTS was anchored onto the BK support by grafting. The typical grafted step carried out was depicted as follows.[33] 1 mL APTS (Aladdin Industrial Co., Shanghai, China) was added in 100 mL toluene followed by addition of 1 g BK support. Then, the mixture was heated to 85 °C under reflux for 16 h, filtered, washed with toluene, and dried at 100 °C for 2 h. The grafted sample was denoted as A-BK-1.

TEPA was anchored onto the A-BK-1 support by impregnating.[34] A certain amount of TEPA (Sinopharm Chemical Reagent Co., Ltd, Shanghai, China) and 0.5 g A-BK-1 were dispersed in 25 mL ethanol and stirred at room temperature (400 rpm, 5 h). After evaporation (80 °C, 8 h) to remove ethanol, the bifunctionalized samples were obtained by drying in a natural convection oven at 100 °C for 1 h, which were referred to A-BK-TEPA-*X* ($X = 30$, 50, 55 or 60), where *X* stands for mass fraction of TEPA. For instance, A-BK-TEPA-30 indicates that the grafted sample A-BK was further loaded with 30 wt% TEPA.

### Experimental method

The adsorption capacity of $CO_2$ on samples was determined by the SDT Q600 thermal gravimetric analyzer (TA, USA). Inlet gas was a mixture of 15 vol% $CO_2$ (99.999%) and 85 vol% $N_2$ (99.999%). Before the adsorption, the thermal gravimetric analyzer needed to be preheated for 1 h. Then a certain amount of A-BK-TEPA-*X* was heated up to 110 °C in a nitrogen atmosphere at a heating rate of 10 °C $min^{-1}$ and kept 40 min to remove the water vapor and other impurity gases to get a constant weight. When the sample temperature recorded by TGA decreased to adsorption temperature (40, 60, 75, 80 and 90 °C), the $CO_2/N_2$ mixed gases were entered until the sample quantity did not change. Finally, the adsorption capacities of samples were calculated using the eqn (1):

$$q_e = \frac{(m_e - m_d)/44.01}{m_d/1000} \quad (1)$$

where $q_e$ is the saturated adsorption capacity of $CO_2$ (mmol $g^{-1}$); $m_e$ and $m_d$ are the weight of adsorption saturated and dewatered adsorbent (mg), respectively; 44.01 is the molar mass of $CO_2$ (g $mol^{-1}$). The cyclic performance of the sample was tested as follows. A certain amount of adsorbent was heated up to 110 °C in a nitrogen atmosphere at a heating rate of 10 °C $min^{-1}$ and kept 40 min to remove the water vapor and other impurity gases to get a constant weight. As cooling to 60 °C, the $CO_2/N_2$ mixed gases were entered until the sample quantity did not change. The cycle was carried out for five times to explore the cyclic performance.

 

### Characterization of samples

X-ray diffraction (XRD) tests were carried out with an X'Pert PRO powder diffractometer (PANalytical, Holland) using Cu-Kα radiation (40 kV and 40 mA) in $2\theta$ range of 0.6–5° and 5–80°. The morphology of each sample was obtained by scanning electron microscopy (SEM) with a scanning electron microscope (Carl Zeiss, Germany) under accelerating voltage of 10 kV. Fourier transform infrared spectra (FTIR) were detected with a Nexus 470 IR spectrometer (Nicolet, USA) in wavenumber interval of 4000–400 $cm^{-1}$. Detected wafers were made by mixing the samples and KBr with a mass radio of 1 : 200. Thermal gravimetric and relevant differential analysis (TGA/DTG) was performed on a SDT Q600 TGA (TA, USA) in nitrogen flow up to 800 °C for A-BK-TEPA-*X*. The nitrogen contents of the samples were detected by EA 2400 II elemental analyzer (Perkin-Elmer, USA), and the average value of three experiments was taken as the test result. Nitrogen adsorption/desorption tests were carried out at −196 °C with a JW-BK200C automatic surface analyzer (JWGB Sci & Tech, Beijing). Each sample was outgassed at 100 °C in vacuum atmosphere for 10 h before test. The surface area was calculated by Brunauer–Emmett–Teller (BET). Total pore volume was calculated from $N_2$ adsorption capacity at $P/P_0 = 0.99$. Pore size distribution of mesopore was derived from adsorption branch of $N_2$ curve using Barrett–Joyner–Halenda (BJH) method.

## Results and discussion

### XRD and SEM characterization

The XRD patterns of KIT-6, Beta, BK and A-BK-1 are presented in Fig. 1. As shown in the small-angle XRD pattern of the synthetic material (Fig. 1a), KIT-6 shows a sharp diffraction peak at $2\theta = 0.88°$, and a shoulder peak after it, corresponding to the (211) and (220) crystal planes of the three-dimensional cubic system.[35] A series of weak peaks of KIT-6 at $2\theta = 1.2–2°$, correspond to (321), (400), (420) and (332) crystal planes. It is clear that the prepared KIT-6 has an ordered three-dimensional cubic mesoporous structure.[36] The composite molecular sieve BK shows the same characteristic peaks as KIT-6, but the intensity of each peak is weakened, which shows that the order of the mesoporous structure of BK decreases. As seen from the wide-angle XRD pattern of the synthetic material (Fig. 1b), the sharp peaks at the degrees of 7.6 and 22.4 in the patterns of all samples are typical reflection of Beta zeolite.[37] The BK and A-BK-1 show a lower intensity in the characteristic peaks compared with Beta because of the existence of KIT-6 phase. In addition, it is possible that the lower crystallinity of zeolite beta in BK is due to the structure degradation in HCl medium. This reason should not be ignored either. These results indicated the well combination of dual pore structures in the composites. Besides, modified by APTS, the mesoporous and microporous structures of BK were not destroyed, but the degree of order decreased. SEM images of Beta, KIT-6, BK and A-BK-1 are shown in Fig. 2. Spherical Beta zeolites with rough surfaces and loose uniform particles were observed (Fig. 2a), whereas KIT-6 displayed smooth surface and the appearance of a bent rod (Fig. 2b). It can be seen the irregular morphology of BK with spherical particles on the surface (Fig. 2c), which was mainly due to the inclusion of Beta microporous molecular sieve into the mesoporous material skeleton, resulting in the uneven grain growth. Fig. 2d shows the BK modified by APTS. Organic amine was loaded onto the carrier, so that the pore channel was filled and the pores between the particles were reduced. However, a certain amount of residual pores still existed, providing a channel for the adsorption and diffusion of $CO_2$.

### FTIR analysis

The FTIR spectra of BK, A-BK-1, A-BK-TEPA-30 and A-BK-TEPA-50 are shown in Fig. 3. All materials showed a broad band near 3467 $cm^{-1}$ due to the physically absorbed water and the stretching vibrations of Si–O.[38] Besides, a sharp band around 1638 $cm^{-1}$ was found, which was due to bending vibration of identical bond as $H_2O$ described above.[39] The bending and symmetric stretching vibration peaks of Si–O–Si in the skeleton were the peaks at 458 $cm^{-1}$ and 790 $cm^{-1}$, respectively, and the anti-symmetric stretching was shown at 1072 $cm^{-1}$.[40] The absorption peaks at 520 $cm^{-1}$ and 570 $cm^{-1}$ were typical characteristic vibration peaks of Beta zeolite five-membered ring and six-membered ring.[37] After APTS modification, the peak intensity of adsorbed water at 1630 $cm^{-1}$ of BK was weakened, because of the methoxy group in APTS reacting with Si–OH to form Si–O–Si bond.[41] The peaks of the amine bifunctionalized

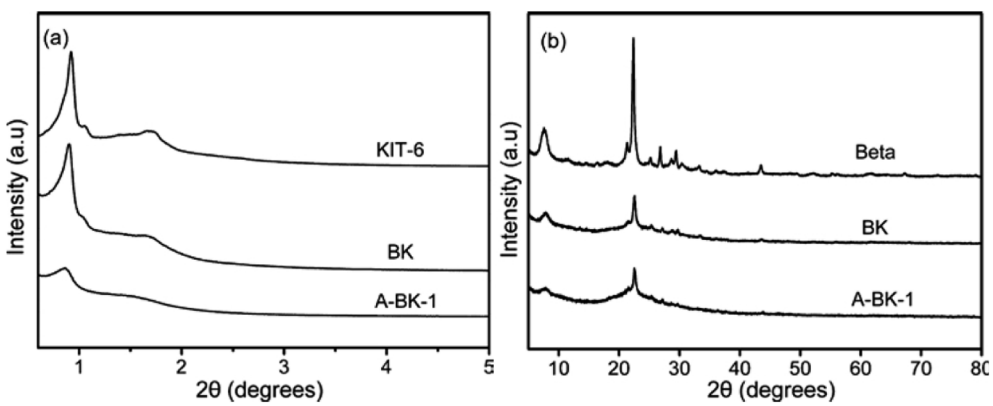


Fig. 1 (a) Small-angle and (b) wide-angle XRD patterns of KIT-6, Beta, BK and A-BK-1.

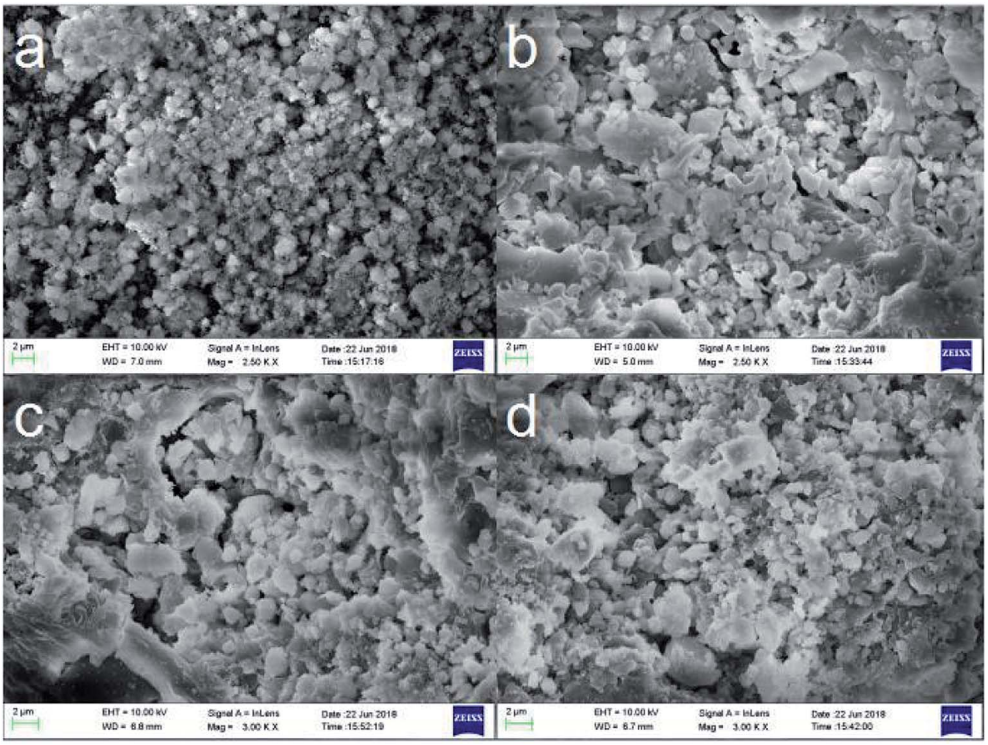


Fig. 2 SEM diagrams of (a) microporous Beta, (b) mesoporous KIT-6, (c) BK and (d) A-BK-1.

BK at 2963 $cm^{-1}$ and 2856 $cm^{-1}$ were the stretching vibration peaks of the C–H bond on the $CH_2$ and $CH_3$ groups in the modifier.[42] The bending vibration peaks of C–H bond and $-NH_2$ were shown at 1482 $cm^{-1}$ and 1569 $cm^{-1}$, respectively, and the stretching vibration peak of C–N bond was 1316 $cm^{-1}$.[43] Compared with the BK modified by grafting alone, it can be seen that with the increase of TEPA impregnation, the peaks at 1482 $cm^{-1}$ and 2963 $cm^{-1}$ were significantly enhanced, and the peak at 1630 $cm^{-1}$ of physically adsorbed water was also enhanced, which was mainly due to the introduction of TEPA improving the ability of the materials to adsorb water. Infrared analysis results showed that TEPA was successfully loaded onto BK grafted by APTS and the modified material and $CO_2$ mainly react as follows:

$$CO_2 + 2RNH_2 \rightarrow RNHCOO^- + RNH_3^+ \quad (2)$$

$$CO_2 + 2R_1R_2NH \rightarrow R_1R_2NCOO^- + R_1R_2NH_2^+ \quad (3)$$

$$CO_2 + R_2NH + RNH_2 \rightarrow R_2NCOO^- + RNH_3^+ \text{ (or } RNHCOO^- + R_2NH_2^+\text{)} \quad (4)$$

## TGA/DTG studies

The thermal stability of composite was determined from the weight loss and the rate of weight loss of the material by TGA/DTG analysis methods for the feasibility of using composite at flue gas temperature. The TGA weight loss curves and the corresponding DTG curves of bifunctionalized BK are shown in Fig. 4. For A-BK-TEPA-*X*, the first obvious weight loss below

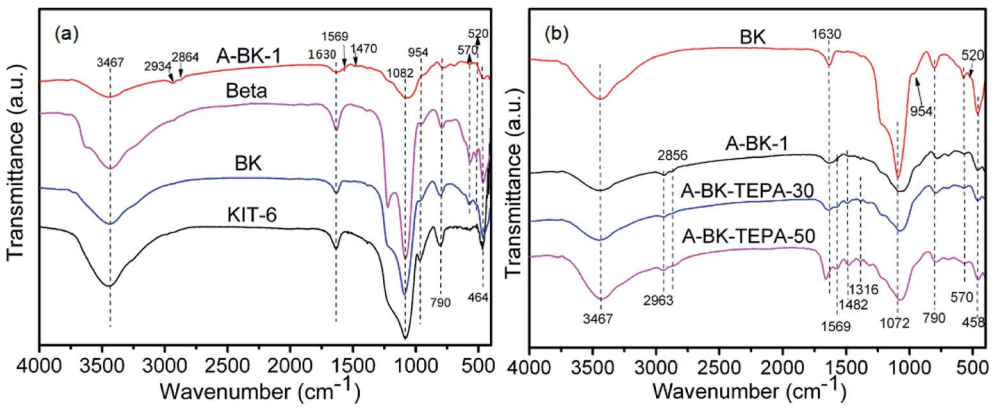


Fig. 3 FTIR spectra of (a) Beta, KIT-6, BK, A-BK-1 and (b) A-BK-TEPA-30 and A-BK-TEPA-50.

 

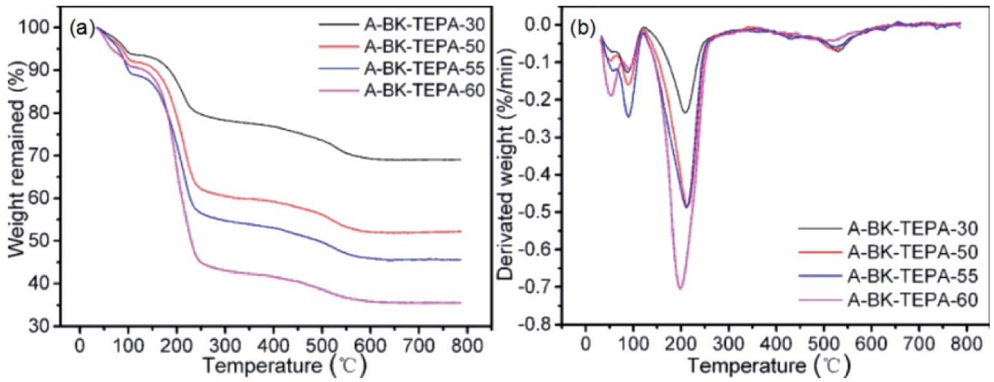


Fig. 4 TGA curves and DTG curves of A-BK-TEPA-*X*.

120 °C was attributed to the impurity gases, physically adsorbed water and residual solvents in the synthesis process (Fig. 4b). The subsequent two stages of weight loss were mainly caused by the decomposition-volatilization of TEPA and APTS and the dehydration of silicon hydroxyl molecules. The materials reach the peak decomposition rate at about 200 °C and the mass variation is no longer obvious after 550 °C. With the same APTS grafting amount, when the TEPA impregnation content increases, the mass loss gradually increases, the intensity of second weightlessness peak slightly increases, and the stability of materials decreases. With impregnating 30%, 50%, 55% and 60% TEPA, the weight losses of the materials were 31%, 48%, 55% and 65%, respectively (Fig. 4a). These weight loss values were all lower than the theoretical value, mainly because APTS and TEPA were not fully loaded on BK during the bifunctionalization process. After filtering or drying, some organic amines were detached from the carrier surface. It can be seen at the TGA/DTG results that the initial decomposition temperature of A-BK-TEPA-*X* was 150 °C, and the double functionalized BK materials can stably exist in the range of adsorption/desorption test temperature (~110 °C).

### $N_2$ adsorption/desorption studies

The $N_2$ adsorption/desorption isotherms of the bifunctionalized BK materials and pore size distribution of KIT-6, BK and A-BK-1 were shown in Fig. 5, and the pore structure data of the material were summarized in Table 1. In Fig. 5a and b, KIT-6, BK, A-BK-1 belonged to the type IV isotherm, showing the type H1 hysteresis ring, which conformed to the adsorption characteristics of mesoporous structure.[44] Beta belonged to the type I isotherm, which was the adsorption characteristic curve of microporous materials. The hysteresis loop height of KIT-6 was higher than that of BK, indicating that its pore volume was larger than that of BK. The results were consistent with the data in Table 1. With the increase of TEPA impregnation amount, the $N_2$ adsorption/desorption isotherm of the composite material BK gradually decreased, and the hysteresis loop also gradually shrank to disappear. The reason was that as the load increased, the amino groups loaded onto the pores and surfaces of BK increased, resulting in the decrease of pore size and $N_2$ adsorbed amount, the disappearance of hysteresis rings, and the pores filling. In Fig. 5c, the pore diameter distribution of KIT-6 was mainly concentrated around 9.84 nm, while the pore diameter distribution of BK was mainly concentrated around 8.56 nm. This was mainly due to the post-synthesis method adopted in this experiment, Beta micropore zeolite was imbedded into the pore channels of the mesoporous molecular sieve KIT-6, resulting in the decrease of pore diameter. However, zeolite Beta does not have mesoporous pore size, which indicated that the prepared composite BK had ordered mesoporous pore channels. In addition, due to the presence of zeolite Beta, the concentration of the pore diameter distribution and pore size of BK materials

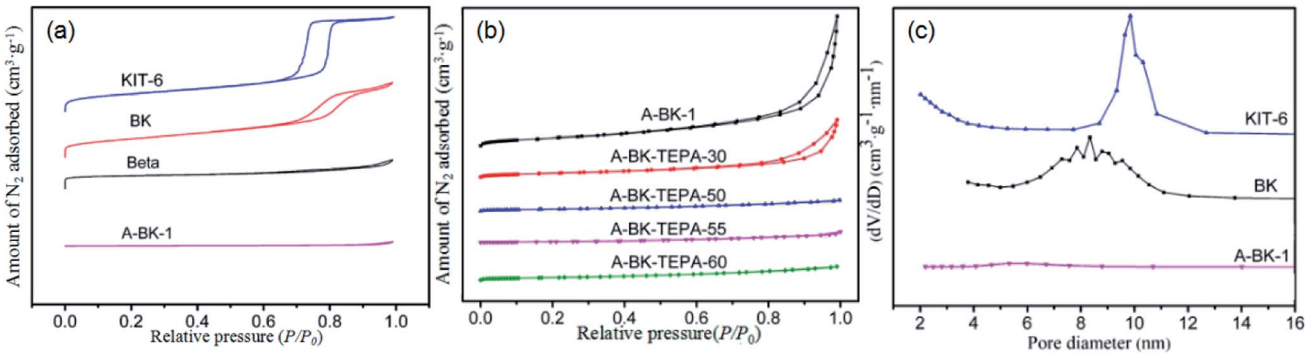


Fig. 5 (a) and (b) $N_2$ adsorption/desorption isotherms and (c) pore size distribution of adsorbents.

Table 1 Physical properties, nitrogen contents, $CO_2$ adsorption capacities and amine efficiencies of adsorbents at 60 °C

| | Pore volume ($cm^3\ g^{-1}$) | Surface area ($m^2\ g^{-1}$) | Mesoporous diameter (nm) | N content (mmol $g^{-1}$) | $CO_2$ adsorption capacity (mmol $g^{-1}$) | Amine efficiency (mmol $CO_2$ $mmol^{-1}$ N) |
|---|---|---|---|---|---|---|
| KIT-6 | 1.42 | 718.5 | 9.84 | — | — | — |
| BK | 1.13 | 655.1 | 8.56 | — | — | — |
| Beta | 0.49 | 545.7 | — | — | — | — |
| A-BK-1 | 0.37 | 120.3 | 5.98 | 5.85 | 2.46 | 0.42 |
| A-BK-TEPA-30 | 0.24 | 96.6 | — | 8.74 | 3.78 | 0.43 |
| A-BK-TEPA-50 | 0.09 | 50.2 | — | 11.39 | 5.12 | 0.45 |
| A-BK-TEPA-55 | 0.07 | 34.7 | — | 12.75 | 4.46 | 0.35 |
| A-BK-TEPA-60 | 0.01 | 9.6 | — | 15.35 | 4.01 | 0.26 |

decreased. After grafting BK with APTS, organic amines were loaded onto the pores and surfaces of the material, blocking some of the pores and making the materials aperture smaller. From the data in Table 1, with the increase of the amino loading capacity, the specific surface area and pore volume of the dual-functional materials decreased rapidly, from 96.6 to 9.6 $m^2\ g^{-1}$ and 0.24 to 0.01 $cm^3\ g^{-1}$, respectively. Besides, the nitrogen content of the BK samples increased from 8.74 to 15.35 mmol $g^{-1}$, whereas the amine efficiency (calculated from eqn (5)) increased first and then decreased.

$$\text{Amine efficiency} = \frac{n_{CO_2}}{n_N} \quad (5)$$

where $n_{CO_2}$ is saturated adsorption capacity of $CO_2$, mmol g; $n_N$ is the molar content of element N, mmol $g^{-1}$.

### Adsorption performance of samples

The $CO_2$ adsorption curves of A-BK-TEPA-*X* at 60 °C are shown in Fig. 6 (inlet $CO_2$ concentration = 15 vol%, gas flow rate = 60 $cm^3\ min^{-1}$). Under the constant grafting amount of APTS, with increasing TEPA loading, the $CO_2$ adsorption capacity increased first and then decreased. Amino functional groups could react with $CO_2$, theoretically the higher the load of impregnated amino group, the higher the adsorption capacity of $CO_2$. However, excessive amino loading on the composite material BK would cause the obstruction of the carrier channel, reduced the specific surface area and pore volume of the materials, hindered the diffusion of $CO_2$ in the material channel and the amino reaction in the pore,[45,46] and reduced the $CO_2$ adsorption ratio to the optimal value. The $CO_2$ saturated adsorption capacity of bifunctionalized adsorbents, A-BK-TEPA-30, A-BK-TEPA-50, A-BK-TEPA-55 and A-BK-TEPA-60, were 3.78, 5.12, 4.46 and 4.01 mmol $g^{-1}$, respectively, and the maximum adsorption capacity was obtained for A-BK-TEPA-50. As an alkanolamine, when APTS was grafted onto a BK carrier, it can provide large amounts of $-NH_2$ adsorption sites. In addition, the silicon hydroxyl groups on BK can react with APTS to form the Si–O–Si network structures, which promoted the dispersion of TEPA, making TEPA more uniformly dispersed in the pores of carriers and providing channels for $CO_2$ diffusion. The synergy of APTS and TEPA on BK carriers improved the $CO_2$ adsorption performance of the adsorbents.

A-BK-TEPA-50 with the best adsorption performance under the same conditions was selected for the further study, and the effect of different adsorption temperatures on the adsorption performance was further investigated. The $CO_2$ adsorption curves of A-BK-TEPA-50 at different temperatures (40, 60, 75, 80 and 90 °C) are described in Fig. 7. The adsorption capacities of

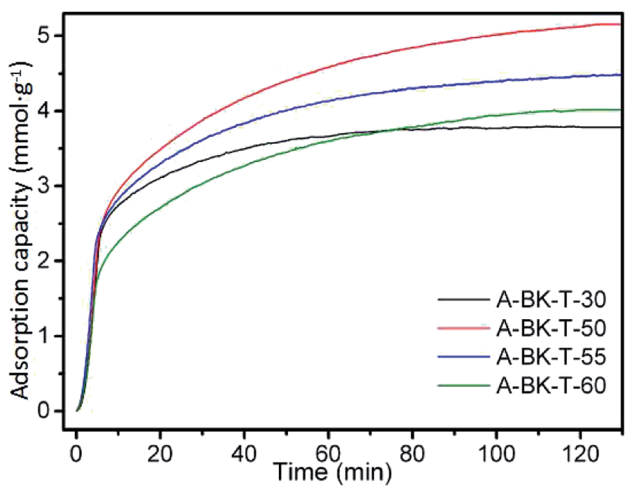


Fig. 6 $CO_2$ adsorption curves of A-BK-TEPA-*X* at 60 °C.

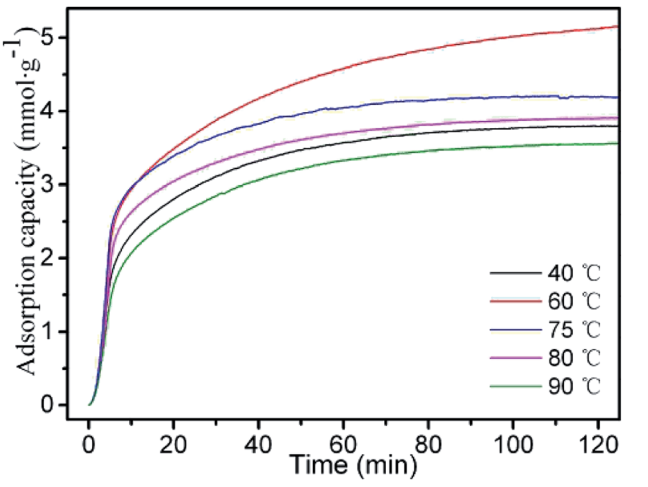


Fig. 7 $CO_2$ adsorption curves of A-BK-TEPA-50 at 40, 60, 75, 80 and 90 °C.

Table 2 $CO_2$ adsorption capacities of various adsorbents from literatures and this experiment

| Support | Modifier (wt) | Condition | Capacity (mmol $g^{-1}$) | Reference |
|---|---|---|---|---|
| MCM-41 | APTS (30%), TEPA (40%) | 15 vol% $CO_2$, 70 °C | 3.50 | 28 |
| SBA-15 | APTS (weight ratio = 1.24), TEPA (30%) | 100 vol% $CO_2$, 45 °C | 2.40 | 29 |
| Pore expanded SBA-15 | APTS, PEI (30%) | 100 vol% $CO_2$, 45 °C | 2.25 | 48 |
| Pore expanded SBA-15 | APTS, TEPA (50%) | 100 vol% $CO_2$, 45 °C | 5.43 | 48 |
| ZSM-5/KIT-6 (ZK) | TMPTA (1 g $g^{-1}$ ZK), TEPA (60%) | 15 vol% $CO_2$, 75 °C | 6.28 | 49 |
| ZSM-5/KIT-6 (ZK) | TMPTA (1 g $g^{-1}$ ZK), PEI (50%) | 15 vol% $CO_2$, 75 °C | 4.69 | 49 |
| Activated carbon (AC) | — | 17 vol% $CO_2$, 55 °C | 0.80 | 50 |
| CNTs | APTS (10%) | 15 vol% $CO_2$, 20 °C | 1.25 | 51 |
| MOF-508 | — | 90.4 vol% $CO_2$, 30 °C | 5.93 | 52 |
| Merlinoite zeolite (MER) | K+ | 100 vol% $CO_2$, 25 °C | 3.50 | 18 |
| Beta/KIT-6 (BK) | APTS (1 mL $g^{-1}$ BK), TEPA (50%) | 15 vol% $CO_2$, 60 °C | 5.12 | This work |

A-BK-TEPA-50 followed the order of 60 °C (5.12 mmol $g^{-1}$) > 75 °C (4.19 mmol $g^{-1}$) > 80 °C (3.90 mmol $g^{-1}$) > 40 °C (3.79 mmol $g^{-1}$) > 90 °C (3.55 mmol $g^{-1}$). From the thermodynamic point of view, the adsorption of $CO_2$ by the dual-functionalized adsorbents was an exothermic reaction, and low temperature was conducive to the $CO_2$ adsorption. However, due to the high viscosity and agglomeration of TEPA on the carriers, the activity of amino groups has an important influence on the $CO_2$ adsorption process. When the adsorption temperature increased, the amino activity of APTS and TEPA and the fluidity of TEPA were enhanced, causing the more uniform distribution of amino groups on the carrier, and more exposed amino active sites, which was beneficial to $CO_2$ adsorption. Besides, with the increase of temperature, the kinetic energy of $CO_2$ molecules increased, benefiting the overcoming of kinetic obstacles, reduction of diffusion resistance, increment of the collision probability with amino active sites, thereby increasing the amount of $CO_2$ adsorption.[47] However, with increasing temperature, the adsorption exothermic reaction process was controlled by thermodynamics. At higher temperatures, $CO_2$ was easily separated from the amino groups, thus the amount of $CO_2$ adsorption was reduced.[21] The condition of 40 °C is more suitable for exothermic reaction, but the $CO_2$ diffusion resistance is higher. The reactivity of amino functional group is stronger at 90 °C, but thermodynamics greatly affects its adsorption performance. The equilibrium between dynamics and thermodynamics is broken. The adsorption capacity of A-BK-TEPA-50 at 40 °C is higher than that at 90 °C, which is possibly due to the volatile decomposition of organic amine molecules at high temperature of 90 °C, which break away from the material surface. Table 2 summarizes the $CO_2$ adsorption capacities of this experiment and other materials. As can be seen from the data in Table 2, although the adsorption capacities of three adsorbents were higher than that of this work, the advantage of amine-bifunctional micro-/mesoporous molecular sieve BK cannot be ignored. The $CO_2$ adsorption conditions of pore expanded SBA-15 (modified by APTS, TEPA) and MOF-508 were 100 vol% and 90.4 vol%, respectively, but ours was only 15 vol%. The higher the concentration of $CO_2$, the better the adsorption effect. However, in this work, 15 vol% $CO_2$ was closer to the $CO_2$ content in the actual flue gas, which can better represent the adsorption performance in the actual application. In addition, MOF materials production method is more complex with high cost. ZSM-5/KIT-6 (modified by TMPTA, TEPA) reacted with $CO_2$ at 75 °C, but our adsorption temperature at 60 °C reduced energy consumption. What's more, the TEPA (60%) dosage was higher than that of this experiment (50%), and the cost of TMPTA was higher than APTS.

To investigate the adsorption mechanism of $CO_2$, the adsorption data of A-BK-TEPA-50 under various temperatures were fitted and analyzed by pseudo-first-order kinetics, pseudo-second-order kinetics[53] and Avrami models[54] according to corresponding eqn (6)–(8):

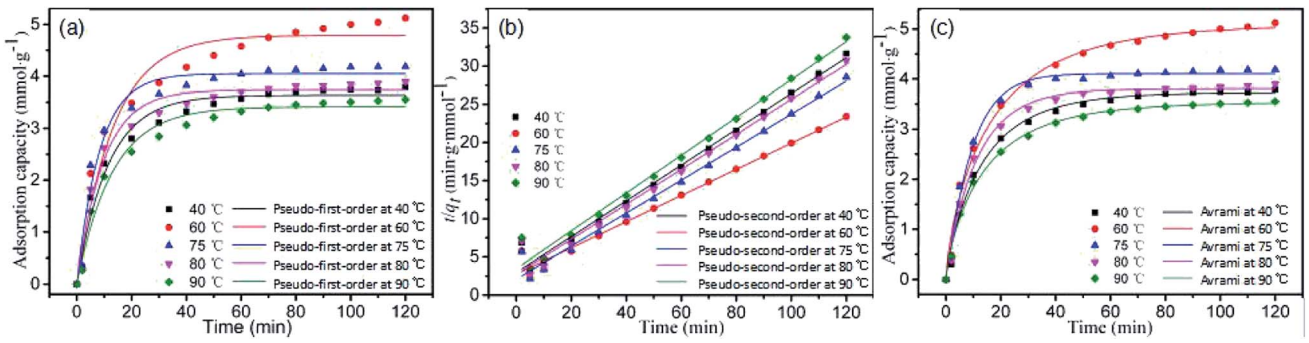


Fig. 8 (a) Pseudo-first-order fitting curves, (b) pseudo-second-order fitting curves and (c) Avrami fitting curves of A-BK-TEPA-50 at various temperatures.

Table 3 Kinetics parameters of adsorption of $CO_2$ on A-BK-TEPA-50 at various temperatures

| Model | Kinetics parameters | 40 °C | 60 °C | 75 °C | 80 °C | 90 °C |
|---|---|---|---|---|---|---|
| Pseudo-first-order | $q_e$ (mmol $g^{-1}$) | 3.64 | 4.79 | 4.05 | 3.74 | 3.41 |
| | $k_1$ ($min^{-1}$) | 0.087 | 0.075 | 0.120 | 0.100 | 0.070 |
| | $R^2$ | 0.976 | 0.962 | 0.968 | 0.973 | 0.978 |
| Pseudo-second-order | $q_e$ (mmol $g^{-1}$) | 4.26 | 5.83 | 4.62 | 4.36 | 4.03 |
| | $k_2$ (g $mmol^{-1}$ $min^{-1}$) | 0.018 | 0.011 | 0.022 | 0.019 | 0.017 |
| | $R^2$ | 0.986 | 0.982 | 0.986 | 0.981 | 0.986 |
| Avrami | $q_e$ (mmol $g^{-1}$) | 3.73 | 5.09 | 4.10 | 3.81 | 3.53 |
| | $k_A$ ($min^{-1}$) | 0.105 | 0.115 | 0.095 | 0.101 | 0.110 |
| | $n_A$ | 0.858 | 0.757 | 0.849 | 0.832 | 0.798 |
| | $R^2$ | 0.990 | 0.991 | 0.993 | 0.992 | 0.996 |

$$q_t = q_e(1 - e^{-k_1 t}) \quad (6)$$

$$t/q_t = 1/(k_2 q_e^2) + t/q_e \quad (7)$$

$$q_t = q_e\left[1 - e^{-(k_A t)^{n_A}}\right] \quad (8)$$

where $q_t$ and $q_e$ are $CO_2$ adsorption capacity of materials at time $t$ and saturated adsorption capacity of $CO_2$, respectively, mmol $g^{-1}$; $k_1$, $k_2$ and $k_A$ are the rate constants of three models, respectively, $min^{-1}$, g $mmol^{-1}$ $min^{-1}$ and $min^{-1}$; $n_A$ is the series of Avrami model.

The fitting results of three kinetics models on A-BK-TEPA-50 are shown in Fig. 8, and the corresponding parameters are shown in Table 3. Comparing the fitting results of three models, the lower fitting degree and the larger deviation between fitted adsorption capacity and experimental data of pseudo-first-order kinetics model and pseudo-second-order kinetics model for A-BK-TEPA-50 at different temperature were found. It is clear that Avrami models were suitable for the description of the adsorption process of A-BK-TEPA-50 at 40, 60, 75, 80 and 90 °C on $CO_2$, and the corresponding correlation coefficients $R^2$ obtained were up to 0.990, 0.991, 0.993, 0.992 and 0.996, respectively. Besides, the saturated adsorption capacities of A-BK-TEPA-50 fitted by these models were very similar to those obtained by experiment. These results suggested that the adsorption of A-BK-TEPA-50 on $CO_2$ is the synergy between physical and chemical adsorption, wherein the chemical adsorption is dominant (the correlation coefficients $R^2$ of the Avrami model and pseudo-second-order kinetics model are both higher than that of pseudo-first-order kinetics model); the nA value changed little, indicating the same adsorption mechanism at different temperatures.

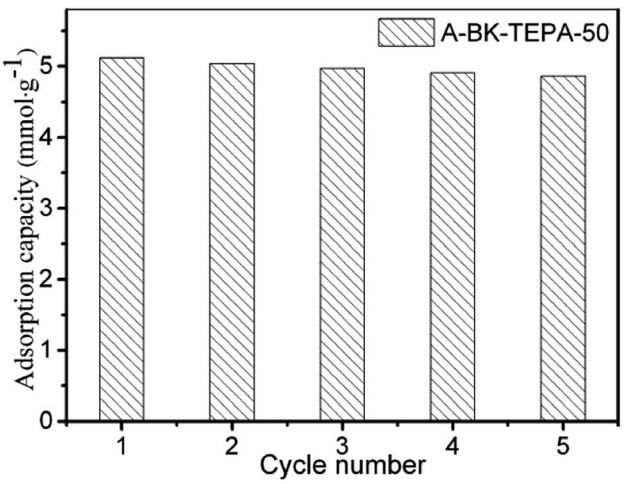


Fig. 9 The $CO_2$ saturated adsorption capacity of A-BK-TEPA-50 during 5 times adsorption/desorption cycles.

### Cyclic adsorption performance of modified samples

The stabilization and reproducibility of an adsorbent are the significant indicators in practical industrial applications. The good regeneration performance of adsorbent can reduce its replacement times, improve its utilization rate and reduce the operating cost of the enterprise. The cyclic adsorption (60 °C, 15 vol% $CO_2$)/desorption (110 °C, $N_2$) performance of A-BK-TEPA-50 was tested by TGA method. The results of five consecutive cyclic adsorption/desorption tests are shown in Fig. 9. After five regenerations, the saturated adsorption capacity of A-BK-TEPA-50 was 4.86 mmol $g^{-1}$, which was only 5.1% less than that of the initial adsorption capacity. This is mainly due to the hydrogen bonding between the amino groups in the APTS and TEPA molecules and the silicon hydroxyl groups in the BK. In addition, the combination of Si–O–Si covalent bonds between the APTS molecules and silicon hydroxyl groups on the BK, as well as the presence of hydrogen bonds and covalent bonds, reduced the loss of TEPA during the heating process, improving the thermal stability and regeneration performance of the adsorbent.

## Conclusions

An amine-bifunctionalized adsorbent was prepared by the APTS grafting and subsequent TEPA impregnation on the micro–mesoporous composite molecular sieve Beta/KIT-6. XRD analysis shows that the micro-/mesoporous composite BK has the three-dimensional cubic mesoporous ordered structure of KIT-6 and the microporous structure of Beta zeolite at the same time, and the structure is not damaged after grafting. The amine efficiency of bifunctionalized materials increases first and then decreases with the amino loading capacity, whereas the specific surface area and pore volume decrease gradually. The

 

adsorption capacities at 60 °C follow the order of A-BK-TEPA-50 (5.12 mmol $g^{-1}$) > A-BK-TEPA-55 (4.46 mmol $g^{-1}$) > A-BK-TEPA-60 (4.01 mmol $g^{-1}$) > A-BK-TEPA-30 (3.78 mmol $g^{-1}$). The adsorption process is the synergy between physical and chemical adsorption, wherein the chemical adsorption is dominant. The regeneration temperature of 110 °C is applicable in the whole adsorption process due to the good thermal stability. The adsorption capacity of A-BK-TEPA-50 exhibited just 5.1% attrition of the original after five adsorption/desorption recycles. The amine-bifunctionalized Beta/KIT-6 adsorbent presented excellent $CO_2$ adsorption/desorption performance, which is expected to offer feasibility for industrial application.

## Conflicts of interest

There are no conflicts to declare.

## Acknowledgements

The authors sincerely acknowledge the support of National Natural Science Foundation of China (No. 51966002) and Natural Science Foundation of Guangxi Province (No. 2020GXNSFAA159144).

## References

1 R. S. Dassanayake, C. Gunathilake, N. Abidi and M. Jaroniec, *Cellulose*, 2018, **25**, 1911–1920.
2 P. Zhao, G. Zhang, Y. Sun and Y. Xu, *Energy Fuels*, 2017, **31**, 12508–12520.
3 R. S. Haszeldine, *Science*, 2009, **325**, 1647–1652.
4 A. Bello and R. O. Idem, *Ind. Eng. Chem. Res.*, 2005, **44**, 945–969.
5 M. Bui, C. S. Adjiman, A. Bardow, E. J. Anthony, A. Boston, S. Brown, P. S. Fennell, S. Fuss, A. Galindo, L. A. Hackett, J. P. Hallett, H. J. Herzog, G. Jackson, J. Kemper, S. Krevor, G. C. Maitland, M. Matuszewski, I. S. Metcalfe, C. Petit, G. Puxty, J. Reimer, D. M. Reiner, E. S. Rubin, S. A. Scott, N. Shah, B. Smit, J. P. M. Trusler, P. Webley, J. Wilcox and N. Mac Dowell, *Energy Environ. Sci.*, 2018, **11**, 1062–1176.
6 Z. F. Lin, X. Tong, W. H. Shen, J. C. Roux and H. X. Xi, *J. Clean. Prod.*, 2020, **244**, 118863.
7 H. T. Hwang, A. Harale, P. K. T. Liu, M. Sahimi and T. T. Tsotsis, *J. Membr. Sci.*, 2008, **315**, 116–124.
8 J. Wang, H. Liang, R. Yang, Z. Zhang, J. Wu, Y. Gao, Q. Wang, D. O'hare and Z. Zhong, *Energy Environ. Sci.*, 2014, **7**, 3478–3518.
9 N. Díez, P. álvarez, M. Granda, C. Blanco, R. Santamaría and R. Menéndez, *Chem. Eng. J.*, 2015, **281**, 704–712.
10 Q. H. Dirar and K. F. Loughlin, *Adsorption*, 2013, **19**, 1149–1163.
11 K. Sumida, D. L. Rogow, J. A. Mason, T. M. Mcdonald, E. D. Bloch, Z. R. Herm, T. H. Bae and J. R. Long, *Chem. Rev.*, 2012, **112**, 724–781.
12 C. Rocha, M. A. Soria and L. M. Madeira, *Sep. Purif. Technol.*, 2019, **235**, 116140.
13 J. C. Abanades, E. S. Rubin and E. J. Anthony, *Ind. Eng. Chem. Res.*, 2004, **43**, 3462–3466.
14 C. Chen, S. S. Kim, K. Cho and W. S. Ahn, *Appl. Surf. Sci.*, 2015, **332**, 167–171.
15 X. Xu, X. Zhao, L. Sun and X. Liu, *J. Nat. Gas Chem.*, 2009, **18**, 167–172.
16 Z. Bao, Y. Liang, D. Tao, Y. Gong and S. Deng, *J. Chem. Eng. Data*, 2011, **56**, 4017–4023.
17 G. Maurin, Y. Belmabkhout, G. Pirngruber, L. Gaberova and P. Llewellyn, *Adsorption*, 2007, **13**, 453–460.
18 M. G. Veselina, E. L. Bruce, C. V. Maarten, R. S. Aaron, J. C. William Jr, B. Stefano and A. W. Paul, *J. Am. Chem. Soc.*, 2019, **141**, 12744–12759.
19 X. Jiang, Y. Zhou, Z. Tang, Z. Chen and Q. Xu, *J. Chem. Pharmaceut. Res.*, 2015, **7**, 363–370.
20 D. Wang, X. Wang and C. Son, *Chemphyschem*, 2017, **18**, 3163–3173.
21 Y. Liu and X. Yu, *Appl. Energy*, 2018, **211**, 1080–1088.
22 C. Zhang, Q. Liu, Z. Xu and K. Wan, *Microporous Mesoporous Mater.*, 2003, **62**, 157–163.
23 Y. Han, S. Wu, Y. Sun, D. Li, F. S. Xiao, J. Liu and X. Zhang, *Chem. Mater.*, 2002, **14**, 1144–1148.
24 W. Guo, L. Huang, P. Deng, Z. Xue and Q. Li, *Microporous Mesoporous Mater.*, 2001, **44**, 427–434.
25 Y. Zhang, Y. Liu and Y. Li, *Appl. Catal. Gen.*, 2008, **345**, 73–79.
26 Z. Lin, J. Wei, L. Geng, D. Mei and L. Liao, *RSC Adv.*, 2017, **7**, 54422–54430.
27 R. Kishor and A. K. Ghoshal, *Microporous Mesoporous Mater.*, 2017, **246**, 137–146.
28 X. Wang, L. Chen and Q. Guo, *Chem. Eng. J.*, 2015, **260**, 573–581.
29 E. S. Sanz-Pérez, A. Arencibia, R. Sanz and G. Calleja, *Adsorption*, 2016, **22**, 609–619.
30 W. J. Son, J. S. Choi and W. S. Ahn, *Microporous Mesoporous Mater.*, 2008, **113**, 31–40.
31 D. Zhang, A. Duan, Z. Zhao and C. Xu, *J. Catal.*, 2010, **274**, 273–286.
32 F. Kleitz, S. H. Choi and R. Ryoo, *Chem. Commun.*, 2003, 2136–2137.
33 R. Kishor and A. K. Ghoshal, *Chem. Eng. J.*, 2015, **262**, 882–890.
34 M. Yue, L. Sun, Y. Cao, Y. Wang, Z. Wang and J. Zhu, *Chemistry*, 2008, **14**, 3442–3451.
35 F. Kleitz, F. Bérubé, C. M. Yang and M. Thommes, *Stud. Surf. Sci. Catal.*, 2007, **170**, 1843–1849.
36 S. Aslam, F. Subhan, Z. Yan, P. Peng, K. Qiao, W. Xing, P. Bai, R. Ullah, U. J. Etim and J. Zeng, *Chem. Eng. J.*, 2016, **302**, 239–248.
37 D. Madden and T. Curtin, *Microporous Mesoporous Mater.*, 2016, **228**, 310–317.
38 Y. Jiang, Q. Gao, H. Yu, Y. Chen and F. Deng, *Microporous Mesoporous Mater.*, 2007, **103**, 316–324.
39 J. Jiao, J. Cao, Y. Xia and L. Zhao, *Chem. Eng. J.*, 2016, **306**, 9–16.
40 S. M. Solberg, D. Kumar and C. C. Landry, *J. Phys. Chem. B*, 2005, **109**, 24331–24337.

41 W. Wang, X. Yang, Y. Fang and J. Ding, *Appl. Energy*, 2009, **86**, 170–174.
42 B. Singh and V. Polshettiwar, *J. Mater. Chem. A*, 2016, **4**, 7005–7019.
43 R. A. Khatri, S. S. C. Chuang, Y. Soong and M. Gray, *Energy Fuels*, 2006, **20**, 1514–1520.
44 Z. Lin, J. Wei, L. Geng, D. Mei and L. Liao, *Water, Air, Soil Pollut.*, 2017, **228**, 412.
45 M. D. Deanna, S. Berend and R. L. Jeffrey, *Angew. Chem., Int. Ed.*, 2010, **49**, 6058–6082.
46 Z. Jian, Z. Hui, L. Jin, Z. Yu, H. Jun, L. Hong and H. Ying, *Solid State Sci.*, 2013, **24**, 107–114.
47 E. Blanchon Le Bouhelec, P. Mougin, A. Barreau and R. Solimando, *Energy Fuels*, 2007, **21**, 2044–2055.
48 R. Sanz, G. Calleja, A. Arencibia and E. S. Sanz-Pérez, *J. Mater. Chem. A*, 2013, **1**, 1956–1962.
49 L. Zhifeng, W. Jianwen, G. Linlin, M. Dejun and L. Lei, *Energy Technol.*, 2018, DOI: 10.1002/ente.201700780.
50 N. Byung-Ki, K. Kee-Kahb, E. Hee-Moon, L. Hwaung and K. S. Hyung, *Korean J. Chem. Eng.*, 2001, **18**, 220–227.
51 S. Fengsheng, L. Chungsying, C. Wenfa, B. Hsunling and F. H. Jyh, *Sci. Total Environ.*, 2009, **407**, 3017–3023.
52 B. Laurent, S. B. Patrick, J. H. Eric, A. C. S. José, E. R. Alírio and C. Banglin, *J. Phys. Chem. C*, 2008, **112**, 1575–1581.
53 Y. X. Wang, B. S. Liu and C. Zheng, *J. Chem. Eng. Data*, 2010, **55**, 4669–4676.
54 K. O. Moura and H. O. Pastore, *Environ. Sci. Technol.*, 2013, **47**, 12201–12210.